The CO anthropogenic emissions in Europe from 2011 to 2021: insights from the MOPITT satellite data.

Audrey Fortems-Cheiney[1,*], Gregoire Broquet[1], Elise Potier[1,**], Robin Plauchu[1], Antoine Berchet[1], Isabelle Pison[1], Hugo Denier van der Gon[2], and Stijn Dellaert[2]

[1]Laboratoire des Sciences du Climat et de l'Environnement, CEA-CNRS-UVSQ, Gif-sur-Yvette, France
[2]Department of Climate, Air and Sustainability, TNO, P.O. Box 80015, 3508 TA Utrecht, Netherlands
[*]now in Science Partners, Quai de Jemmapes, 75010 Paris, France
[**]now in Laboratoire Inter-universitaire des Sciences Atmosphériques, Univ Paris Est Créteil and Université Paris Cité, CNRS, LISA, 94010 Créteil, France

Correspondence: Audrey Fortems-Cheiney, audrey.fortems@science-partners.com

Abstract. We have used the variational inversion drivers of the recent Community Inversion Framework (CIF), coupled to a European configuration of the CHIMERE regional chemistry transport model and its adjoint to derive carbon monixide (CO) emissions from the MOPITT TIR-NIR observations, for a period of over 10 years from 2011 to 2021. The analysis of the inversion results reveals the challenges associated with the inversion of CO emissions at the regional scale over Europe. Annual budgets of the national emissions are decreased by about 1-11% over the decade and across Europe. These decreases are mainly due to negative corrections during autumn and winter. The posterior CO emissions follow a decreasing trend over the European Union + United Kingdom area with a trend of about -2.2 %/year, slightly lower than in the prior emissions. The assimilation of the MOPITT observation in the inversions indeed attenuates the decreasing trend of the CO emissions in the TNO inventory over areas benefiting from the highest number of MOPITT super-observations (particularly over Italy and over the Balkans), and particularly in autumn and winter. The small corrections of the CO emissions at national scales by the inversion can be attributed, first, to the general consistency between the TNO-GHGco-v3 inventory and the satellite data. Analysis of specific patterns such as the impact of the covid-19 crisis reveal that it can also be seen as a lack of observation constraint to adjust the prior estimate

of the emissions. The large errors **associated to the observations in our inversion framework**, and the lack of data over large parts of Europe are sources of limitation on the observational constraint. Emission hot spots generate a relatively strong local signal, which is much better caught and exploited by the inversions than the larger scale signals, despite the moderate spatial resolution of the MOPITT data. This is why the corrections of these hot spot emissions are stronger and more convincing than the corrections of the national and continental scale emissions. Accurate monitoring of the CO national anthropogenic emissions may thus require modeling and inversion systems at spatial resolution finer than those used here, as well **as** satellite images at high spatial resolution. The CO data of the TROPOMI instrument onboard the Sentinel-5P mission should be well suited for such a perspective.

Plain Language Summary

1 Introduction

Carbon monoxide (CO) is an air pollutant and a greenhouse gas, mainly emitted by anthropogenic activities, and impacting both the air quality and climate change. It has a major role in atmospheric chemistry, as a key component of the methane (CH_4) oxidation chain with formaldehyde (HCHO), ozone (O_3), and carbon dioxide (CO_2). Through chemical interactions with hydroxyl radical (OH), CO i) influences concentrations of CH_4 and non-methane volatile organic compounds (NMVOCs), ii) affects the self-cleaning or oxidation capacity of the atmosphere (Lelieveld et al., 2016) and iii) leads to the chemical production of air pollutants and/or greenhouse gases such as tropospheric O_3 and CO_2. In this context, there is a need for an accurate mapping/monitoring of the CO surface emissions.

CO emissions estimated by bottom-up (BU) inventories, based on statistical and economic data and relying on emission factors per activity type, suffer from relatively large uncertainties. For example, at the national and annual scales, these uncertainties range from 20-60% to 50-200% depending on the sectors in the European Monitoring and Evaluation Programme (EMEP) inventory (Kuenen and Dore, 2019). Complementary to BU inventories, atmospheric CO concentration data, such as those observed from satellite observations, can be used to derive estimates of the CO fluxes, based on atmospheric transport inverse modeling techniques (Rayner et al., 2019). Over the last two decades, the space-borne Measurement of Pollution in the Troposphere (MOPITT,

(Drummond et al., 1996; Deeter et al., 2003), the Atmospheric Infrared Sounder (AIRS, (Aumann et al., 2003; McMillan et al., 2005), Tropospheric Emissions Spectrometer (TES, (Beer, 2006) and Interféromètre Atmosphérique de Sondage dans l'Infrarouge (IASI, (Clerbaux et al., 2009)) have revolutionized our ability to map CO concentrations and to understand the trends **and the spatio-temporal variability** of its concentrations and emissions **(Arellano et al., 2006; Chevallier et al., 2009; Jones et al., 2009; Kopacz et al., 2010; Jiang et al., 2011; Fortems-Cheiney et al., 2011a; Hooghiemstra et al., 2012; Miyazaki et al., 2015; George et al., 2015; Yin et al., 2015; Jiang et al., 2017; Zheng et al., 2018; Buchholz et al., 2021; Gaubert et al., 2023).** However, the potential of satellite data to inform about CO emissions has been mainly explored at the global scale, with emission estimates corresponding to large regions. Today, the scientific and societal issues require an up-to-date quantification of pollutant emissions at a higher spatial resolution, targeting national estimates. This currently requires the use of regional scale inversion systems (Fortems-Cheiney et al., 2021).

However, although these systems are suited to reactive species, they have hardly been used to quantify emissions of pollutants such as CO. **In the past decade, CO regional scale inversions based on the MOPITT data covered the CO emissions in North America (Jiang et al., 2015) and East Asia (Qu et al., 2022). To our knowledge, there has been only few studies covering the European CO emissions based on satellite observations (Konovalov et al., 2016; Fortems-Cheiney et al., 2021), this continent being more challenging for regional scale inversions of the CO anthropogenic emissions owing to a weaker CO signal (Konovalov et al., 2016).** Konovalov et al. (2016) estimated CO European emissions from the IASI thermal-infrared (TIR) satellite measurements over Europe **but** pointed out the low sensitivity of the corresponding CO total columns to anthropogenic CO emissions. Deeter et al. (2013) have shown that the sensitivity of total columns to CO emissions in the lower troposphere - where the regional signal from CO regional anthropogenic emissions above the large scale and highly mixed CO background is the largest - should be significantly greater for retrievals exploiting simultaneous TIR and near-infrared (NIR) measurements than for retrievals based on either spectral region alone. Fortems-Cheiney et al. (2021) have performed regional inversions using MOPITT TIR-NIR satellite observations over Europe to illustrate the behavior of the variational atmospheric inversion system PYVAR-CHIMERE, but only over a short temporal window of seven days. The ability of

regional inverse systems to quantify CO budgets at the national **and monthly to annual scales in Europe** from the MOPITT TIR-NIR satellite observations has not been assessed yet.

The objective of this work is therefore to carry out a long-term regional inversion for Europe using these observations. We estimate CO emissions from the MOPITT TIR-NIR observations, for more than 10 years from January 2011 to November 2021. The analysis over the period 2011-2021 makes it possible to evaluate the strong trends indicated by the BU inventories over the decade, and major inter-annual anomalies, in particular the expected reduction of emissions in 2020 due to the measures taken in response to the COVID-19 pandemia. For this objective, we have used the variational inversion drivers of the recent Community Inversion Framework (CIF, (Berchet et al., 2021)), which inherits the developments made for the regional assimilation of satellite data on gaseous species by Fortems-Cheiney et al. (2021). We also use a European configuration of the CHIMERE regional chemistry transport model (CTM) (Menut et al., 2013; Mailler et al., 2017) and of its adjoint (Fortems-Cheiney et al., 2021), driven by the CIF. The data and methods used in this study are described in Section 2. The results are described in Section 3.

2 Data and Methods

2.1 Configuration of the CHIMERE CTM for the simulation of CO concentrations in Europe

The configuration of the atmospheric CTM CHIMERE for Europe is described in Table 1. CHIMERE is run over a $0.5° \times 0.5°$ regular horizontal grid and 17 vertical layers, from the surface to 200hPa, with 8 layers within the first two kilometers. The domain covers Europe (15.25°W-35.75°E; 31.75°N-74.25°N) and includes 101 (longitude) x 85 (latitude) grid-cells. The reanalyzes ERA-Interim – the only ones available at the beginning of this study - remain at the rather low horizontal resolution of 79 km compared to the forecast fields. Consequently, as a trade-off between accuracy of large-scale meteorological fields and resolution at finer resolution, CHIMERE is driven here by the European Centre for Medium-Range Weather Forecasts (ECMWF) operational meteorological forecast (Owens and Hewson, 2018), with a spatial resolution of 0.25°. The chemical scheme used in CHIMERE is MELCHIOR-2, with more than 100 reactions (CHIMERE, 2017), including the secondary production of CO through the oxidation and photolysis of hydrocarbons and its sink with OH.

Initial and boundary conditions for several key gaseous species responsible for the oxidation capacity of the lower atmosphere (e.g., CO, NO, NO_2, O_3,H_2O_2, HCHO, etc) were specified using monthly climatological data from LMDz-INCA global model (Szopa, 2008).

Domain	Europe (15.25°W-35.75°E; 31.75°N-74.25°N)
Horizontal resolution	0.5°×0.5° regular grid
Vertical resolution	17 layers, from the surface to 200hPa
Meteorological fields	ECMWF operational meteorological forecast (Owens and Hewson, 2018)
Initial and boundary conditions	Climatological values from the LMDZ-INCA global model (Szopa, 2008)
Anthropogenic emissions	TNO-GHGco-v3 inventory (Super et al., 2020)
Biogenic emissions	MEGAN (Guenther et al., 2006)

Table 1. *Main characteristics of the European CHIMERE configuration used in this work.*

CO emissions from fires, that count for about 2% of the European total COemissions (San-Miguel-Ayanz and Steinbrecher, 2019), are not taken into account in this study. CO biogenic emissions are assumed to be negligible and are not taken into account. **Contrarily to Fortems-Cheiney et al. (2021) using the TNO-GHGco-v1,** the prior estimate of CO anthropogenic emissions is derived from the recent TNO-GHGco-v3 gridded inventory for the period 20**11**-2018. The TNO-GHGco version is an update of the TNO inventory (Super et al., 2020; Denier van der Gon et al., 2021; Kuenen et al., 2022) based on EMEP/CEIP official country reporting for air pollutants. This inventory has been delivered with an extrapolation of the emissions for the year 2019, based on an in-sample approach (Super et al., 2020). We use this combination of products for the years 20**11**-2019. Our prior estimates of the emissions for 2020 and 2021 are set at the values for 2019. The horizontal resolution of the TNO-GHGco-v3 inventory is 6x6 km^2. **The TNO-GHGco inventory combines emissions from area sources, set at the surface, and from point sources. Emissions from point sources, mainly from the energy production and the industrial sector, are distributed on the vertical model layers depending on typical the injection height provided in the TNO inventory, based on Bieser et al. (2011)**. The annual and national budgets from EMEP/CEIP are disaggregated in space based on proxies of the different sectors of activity (Kuenen et al., 2022). The temporal disaggregation is based on temporal profiles provided per

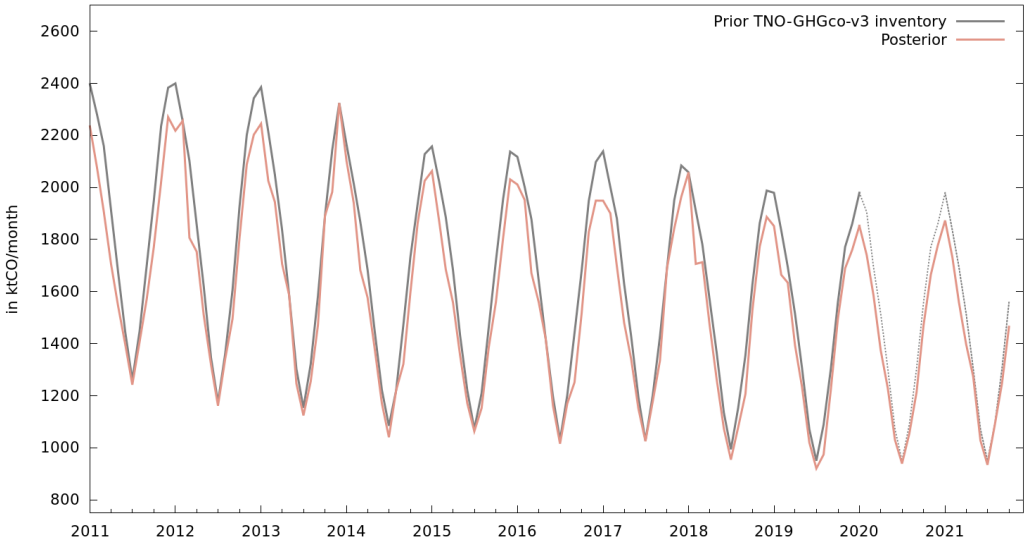

Figure 1. *Estimates of the monthly budgets of CO for EU-27+UK from the TNO-GHGco-v3 inventory (solid light grey line) and its extension to 2020-2021 (dashed light grey line), and from the regional inversions (solid orange line), from January 2011 to December 2021.*

GNFR sector code with typical month to month, weekday to week-end and diurnal (at 1-hour scale) variations. The TNO-GHGco-v3 inventory is aggregated at the 0.5°x0.5° horizontal resolution of the CHIMERE grid. The resulting prior anthropogenic CO emissions **from 2011 to 2021 for the European Union + United Kingdom (EU-27+UK) area are illustrated in Figure 1 and the resulting map of prior anthropogenic CO emissions is shown in Figure 2a for January 2015**. CO emissions are high over large cities and over industrial areas (e.g. over the Benelux, the Po Valley in Italy, northwestern Germany, southern Poland).

In addition to CO, the chemical scheme MELCHIOR-2 needs emissions from other species, such as NMVOCs or nitrogen oxides (NO_x=NO+NO_2). Anthropogenic NO_x emissions are from the TNO-GHGco-v3 inventory while NMVOC anthropogenic emissions are from the EMEP inventory (Vestreng et al., 2005). Biogenic NO_x and NMVOC emissions, in particular emissions of isoprene and some other hydrocarbons from vegetation, are obtained from the Model of Emissions of Gases and Aerosols from Nature (MEGAN) model (Guenther et al., 2006).

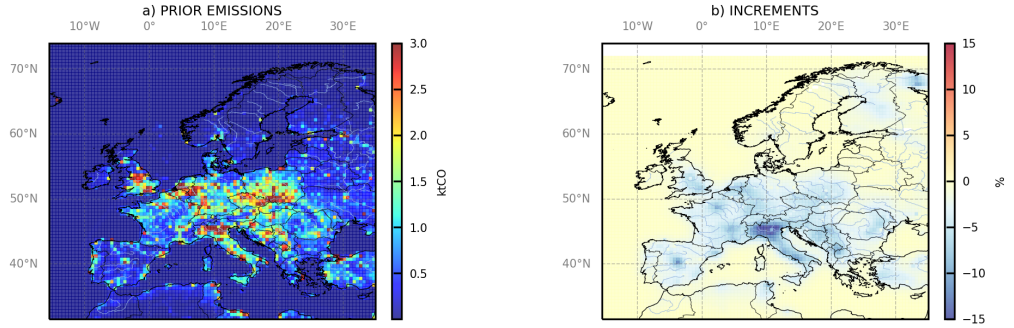

Figure 2. a) Monthly CO emissions in ktCO, and b) monthly mean relative increments to the TNO-GHGco-v3 inventory of CO anthropogenic emissions from the inversion in %, in January 2015, at the 0.5°×0.5° model resolution.

The resulting monthly **mean volume mixing ratio between the surface and 900 hPa are illustrated in Figure 3a in January 2015.** The sensitivity of CO simulated concentrations to CO emissions is evaluated by running a sensitivity test with European CO anthropogenic emissions set to zero: the simulated concentrations are illustrated in Figure 4.

2.2 MOPITT satellite observations

CO inversions assimilate CO observations from the MOPITT **retrieval product version 8** (Deeter et al., 2019). MOPITT flies onboard the NASA EOS-Terra satellite, on a low sun-synchronous orbit that crosses the Equator at 10:30 and 22:30 local solar time (LST). The spatial resolution of its observations is about 22×22 km^2 at nadir. It has been operated nearly continuously since March 2000. MOPITT CO products are available in three variants: thermal-infrared TIR only, near-infrared NIR only and the multispectral TIR-NIR product, all containing total columns and retrieved profiles (given on a 10-level grid from the surface to 100 hPa). Among the different MOPITTv8 products, we choose to work with the multispectral MOPITTv8-NIR-TIR one (also called MOPITT-v8J), as the sensitivity to CO in the lower troposphere should be significantly greater for retrievals exploiting simultaneous TIR and NIR measurements than for retrievals based on either spectral region alone **(Worden et al., 2010; Deeter et al., 2013; Buchholz et al., 2017)**. In addition, it provides the highest number of data.

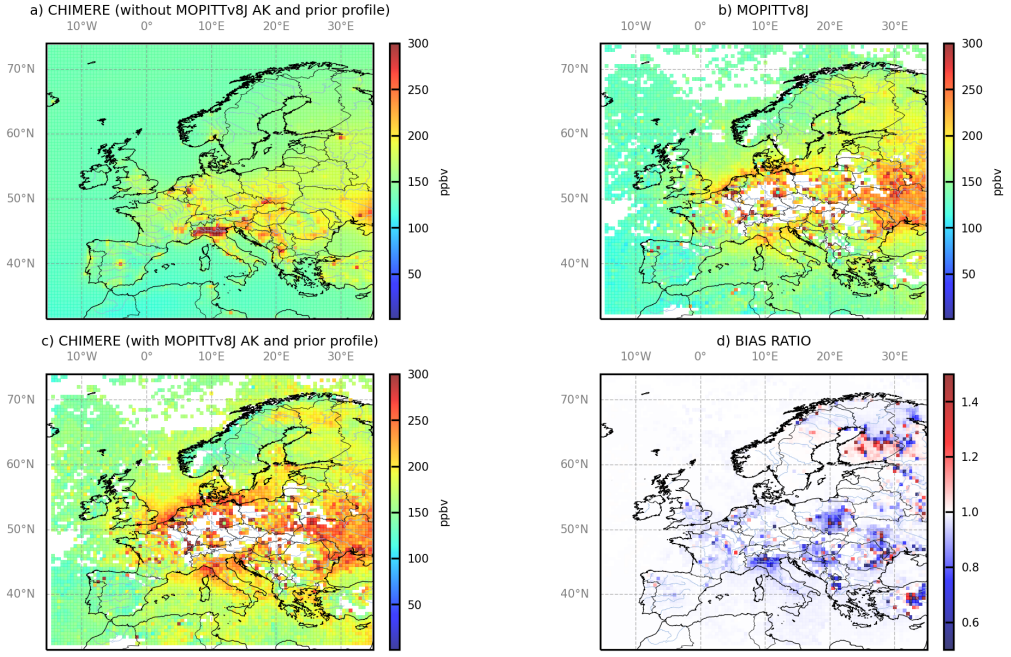

Figure 3. *Averages of the CO concentrations between the surface and 900 hPa, a) simulated by CHIMERE using the prior TNO-GHGco-v3 anthropogenic emission estimate without applying the MOPITT AK and prior profiles, b) corresponding to the MOPITT surface super observations in the CHIMERE grid, c) simulated by CHIMERE using the prior TNO-GHGco-v3 anthropogenic emission estimate applying the MOPITT AK and prior profiles, in ppbv. d) Ratios of the posterior and prior biases between monthly mean surface concentrations from CHIMERE and the MOPITT super-observations, at the 0.5°x0.5° grid-cell resolution, in January 2015. All ratios lower than 1, in blue, demonstrate that posterior emission estimates improve the simulation compared to the prior ones.*

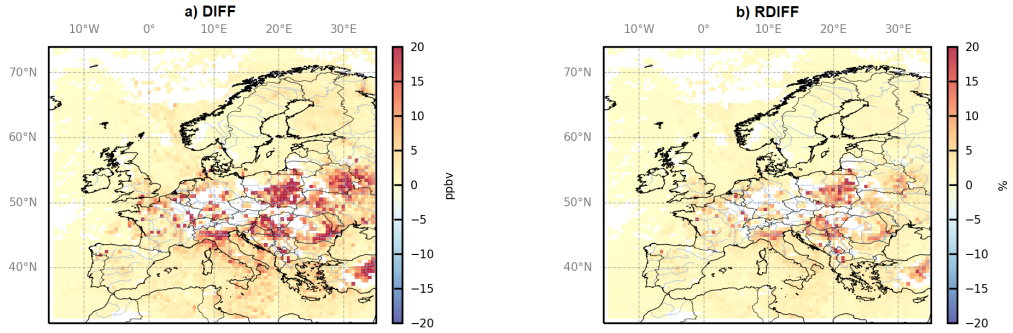

Figure 4. ***a) Absolute differences in ppbv and b) relative differences in % between averages of CO concentrations simulated using the prior TNO-GHGco-v3 anthropogenic emission estimate and simulated with null CO emissions, in January 2015.***

We choose to assimilate the MOPITT V8J surface product, **derived as the mean volume mixing ratio between the surface and 900 hPa, as the surface level multispectral retrievals have greater sensitivity to CO near the surface and reduced sensitivity in the free troposphere (Jiang et al., 2015; Qu et al., 2022). Long-term trends of surface CO concentrations for 2001–2015 are well consistent between the « MOPITT lower profile » and World Data Center for Greenhouse Gases (WDCGG) sites (Jiang et al., 2017). The retrieval bias drift is also low at the surface level for v8 TIR–NIR products, as compared to National Oceanic and Atmospehric Administration (NOAA) flask measurements (Deeter et al., 2019). Finally, the surface level of the V8 TIR–NIR products gives the lowest bias when compared to in situ data from NOAA aircraft validation sites (Deeter et al., 2019).**

To make accurate comparisons between simulations and satellite observations, the averaging kernels (AKs) and the MOPITT prior profiles are applied to the simulated field so that the simulated concentrations exhibit the same degree of smoothing and a priori dependence as the MOPITT product (Deeter et al., 2013, 2019). Following the recommendations of Deeter (2018), the formula is applied :

c_m=$\mathbf{x}_a$ + **AK**($\mathrm{c}_m{}^\circ$ - $\mathbf{x}_a$)$(Eq1)$

where:

- $\mathbf{c}_m$ **is the modeled column,**

- **AK contains the averaging kernels -which are an indication of the vertical resolution of the measurements- provided in the form of a matrix,**
- **$\mathbf{x}_a$ is the prior profile derived from a model climatology and vary seasonally and geographically (Deeter et al., 2019)**
- **and $\mathbf{c}_m{}^\circ$ is the vertical distribution of the original model partial columns interpolated to the pressure grid of the AKs.**

In order to associate the super-observations to a real AK, the super-observations have been taken as the individual observation corresponding to the value of the median of the MOPITT concentrations within the $0.5° \times 0.5°$ grid-cell of the CTM and within the CTM physical time steps (about 5-10 min). **The AKs and the uncertainty associated to this individual super-observation are then used to define the AK and uncertainty for the "super-observation". In principle, the observation error associated to such a median value should be smaller than the error associated to individual observation, but, here, we keep the error for the individual observation used to define the super-observation as a conservative estimate of the super-observation error. The super-observations therefore do not have a smaller error than the individual observations.**

The resulting monthly means of the MOPITT super-observations and their simulated equivalents for CO average surface concentrations in January 2015 are respectively illustrated in Figure 3b and in Figure 3c. The spatial patterns of the CO concentrations are very different if the MOPITT AK and prior profiles are applied (Figure 3a) or not (Figure 3b), particularly in Central, Eastern and Northern Europe. It bears evidence that the MOPITT AK and prior profiles have a strong impact on the CO concentrations over these regions.

It is important to note that the potential of MOPITT to provide information can be strongly hampered by the cloud coverage in autumn and in winter, as illustrated in Figure 3**b** with blanks for a large part of Central Europe in January 2015. Generally, because of the cloud cover, the number of MOPITT super-observations is higher in the south of Europe than in Central or Northern Europe (Figure 5a). **The potential of MOPITT to provide information can also be hampered by the errors associated to the MOPITT super-observations (Figure 5b, see Section 2.2**).

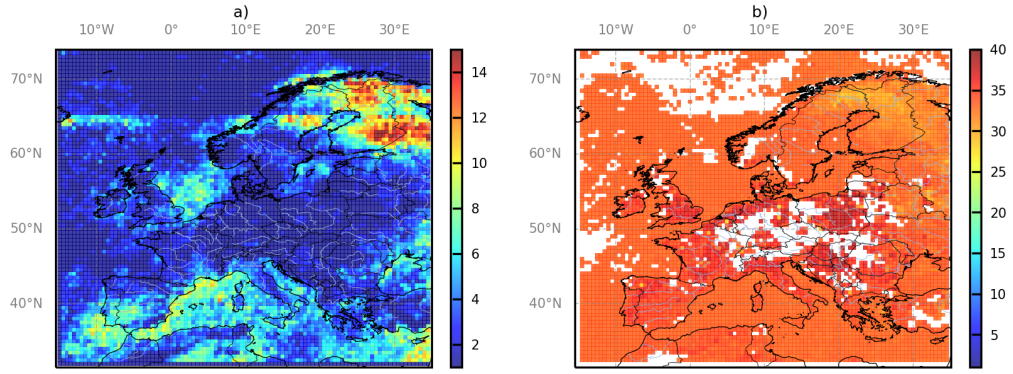

Figure 5. *a) Number of CO MOPITT super-observations and b) Averages of the errors associated with the CO MOPITT super observations, in %, in January 2015.*

2.3 Variational inversion of CO anthropogenic emissions

The inversion of CO emissions consists in correcting the "prior" estimate of these emissions and of the model initial and/or boundary conditions to improve the fit between the simulated concentrations and the satellite CO data. The parameters of the variational inversions here closely follow the configuration of Fortems-Cheiney et al. (2021), which provides details on on the principle and configuration for such inversions. The optimal ("posterior") estimate of the emissions in a statistical sense is found by iteratively minimizing the following cost function $J(\mathbf{x})$:

$$J(\mathbf{x}) = \frac{1}{2}(\mathbf{x}-\mathbf{x}^b)^T\mathbf{B}^{-1}(\mathbf{x}-\mathbf{x}^b) + \frac{1}{2}(\mathcal{H}(\mathbf{x})-\mathbf{y})^T\mathbf{R}^{-1}(\mathcal{H}(\mathbf{x})-\mathbf{y})$$

where $\mathbf{x}$, $\mathcal{H}$, $\mathbf{y}$, $\mathbf{B}$, $\mathbf{R}$ are respectively the control vector, the observation operator, the observations, and covariance matrices as detailed in the following paragraphs.

As a trade-off between computational resources and relevance of our inversions with a moderate impact of the initial conditions on our 1-month CO simulation, series of **independent** 1-month inversion windows are run. **We therefore do not account for the potential update of the concentrations during a previous 1-month window due to the inversions.** Due to the relatively long lifetime of CO -i.e., few weeks to 2 months (Prather, 1996)- compared to the size of the studied domain, we account for the CO lateral boundary conditions at the borders of the domain and for their uncertainties.

Therefore, the control vector $\mathbf{x}$ contains:

- CO anthropogenic emissions at a 1-day temporal resolution, at a 0.5°×0.5° resolution and over the first 8 vertical levels of CHIMERE, i.e., for a one-month inversion, for each of the corresponding (28 to 31 days)×101×85×8 grid cells. **The 8 levels are needed to represent the range of injection heights for the largest point sources, (e.g., mainly for the energy production and industrial sector) provided in the TNO emission inventory**,

- CO lateral boundary conditions at a 1-day temporal resolution, at a 0.5°×0.5° resolution and over the 17 vertical levels of CHIMERE, i.e. for each of the corresponding (28 to 31 days)×372×17 grid cells,

- CO 3D initial conditions at 00:00 UTC the first day of the month, at a 0.5°×0.5° resolution and over the 17 vertical levels of CHIMERE, i.e. for each of the corresponding 101×85×17 grid cells.

It should be noted that the VOCs emissions are fixed and not controlled here by the inversion. Nevertheless, the chemical production of CO by VOCs could be changed due to the correction of CO boundary conditions and fluxes through chemistry.

$\mathcal{H}$ is the observation operator, which links the control variables to the observed concentrations; it includes the CTM, space and time sampling and other operations (e.g averaging) required to compute the simulated equivalent of the assimilated data. The uncertainties in the observations $\mathbf{y}$ together with that in the observation operator $\mathcal{H}$, and the uncertainties in the prior estimate of the control vector $\mathbf{x}^b$ are assumed to have a Gaussian distribution and are thus characterized by their covariance matrices $\mathbf{R}$ and $\mathbf{B}$, respectively. The assumptions and practical way to define these matrices have been detailed by Fortems-Cheiney et al. (2021). The ratios between the prior error standard deviations in $\mathbf{B}$ and the prior estimates are assigned to 100% for the CO emissions. **This value of 100% has already been chosen in the literature (Pétron et al., 2002; Kopacz et al., 2010; Yumimoto and Uno, 2006; Fortems-Cheiney et al., 2011b, 2012, 2021). Even though annual CO emissions in western Europe may be well known, with uncertainties of 6% according to Super et al. (2020), larger uncertainties could affect eastern Europe. Moreover, large uncertainties still affect bottom-up emission inventories at the 0.5° resolution: spatial disaggregation of the national-scale estimates to provide gridded estimates causes a significant increase in the uncertainty for CO (Super et al., 2020).**

Contrarily to Fortems-Cheiney et al. (2021) where they are set to 15%, the ratios between the prior error standard deviations in **B** and the prior estimates are set at 50% for the CO lateral conditions. Spatial correlations are built with exponentially decaying functions with an e-folding length of 50 km on land and on sea. Here, the covariance matrix **R** only takes into account the estimates of measurement errors reported in the MOPITT data sets. Indeed, the errors associated to the observation operators (in particular those associated to the chemistry-transport modelling with the CHIMERE configuration for Europe) are ignored since they are assumed to be much smaller than those associated to the MOPITT data. The minimum of the cost function J is searched for with the iterative limited-memory quasi-Newton minimization algorithm M1QN3 algorithm (Gilbert and Lemaréchal, 1989). At each iteration, the computation of the gradient of J relies on the adjoint of the observation operator, and in particular on the adjoint of CHIMERE. In the results presented in Section 3, the norm of the gradient of the cost function J is reduced by more than 90%, which indicates robust mathematic behaviour of the system.

The calculation of the uncertainty in the estimate of emissions from the inversion, known as "posterior uncertainty", is challenging when using a variational inverse system (Rayner et al., 2019): it is not done here.

3 Results

3.1 Comparison between simulated and assimilated CO concentrations

The MOPITT data and their prior simulated equivalents present similar spatial patterns for CO concentrations, with lowest values over Spain (i.e., with about 125 ppbv) and values higher than 200 pbbv over Central Europe (over the Benelux, the Po Valley in Italy, northwestern Germany, southern Poland, Figure 3). However, the prior simulation overestimates CO concentrations compared to the MOPITT super-observations, in particular over urban and industrial areas in central Europe, where the anthropogenic emissions are large (Figure 2a).

It is interesting to note that global models have struggled with a low bias in CO in the Northern Hemisphere, particularly in winter, compared to the MOPITT observations (Fortems-Cheiney et al., 2011a; Stein et al., 2014). However, compared to these previous studies, we have used more recent MOPITT observations and validation results for version 8 MOPITT CO products indicate reduced long-term bias drift, weaker bias geographical variability

and smaller biases overall compared to version 7 (Deeter et al., 2018). We have also used a more recent prior estimation of the CO emissions from the TNO-GHGco-v3 inventory, as it is based on recent EMEP/CEIP official country reporting for air pollutants. As model errors in long-range transport, diffusion, chemistry linked to the radical hydroxil OH and to NMVOCs (Strode et al., 2015; Gaubert et al., 2020) and coarse resolution (Valin et al., 2011) can all impact the inverse modeling of CO (Arellano et al., 2006; Fortems-Cheiney et al., 2011a; Jiang et al., 2017; Zheng et al., 2019), we also used a chemical scheme describing the CO chemistry (including its secondary production through the oxidation and photolysis of hydrocarbons and its sink with OH, Section 2.1) and we have increased the spatial resolution of the transport model with a regional CTM. These different aspects can explain that our regional inversion do not highlight a low bias in the inventories, unlike past global inversions studies.

By design, the inversions bring the simulated CO concentrations closer to the MOPITT "surface" super-observations (Figure 3d). **The mean bias over the entire domain between the simulation and the MOPITT super-observations is reduced by about 2%. Nevertheless,** the corrections made to the prior TNO-GHGco-v3 inventory are particularly large in areas where both CO emissions and the sensitivity of CO concentrations to the emissions are high (Figure 2a, Figure 4). For example, the posterior emissions reduce the mean bias between simulated concentrations and MOPITT data by about 26% over the Po Valley in Italy and over Benelux in January 2015 (Figure 3d).

Nevertheless, it is worth stressing that the posterior simulation still presents positive biases compared to the observations (Figure 3d). This can be explained by i) large errors in the MOPITT **super-**observations that could reach 40% (Figure 5b) and ii) by the relatively weak sensitivity of the simulated concentrations to the local/regional emissions, as illustrated in Figure 4.

3.2 Posterior CO emissions

This section focuses on the emissions from the 11-year CO inversion for the period 2011 to 2021. As the prior simulation overestimates CO concentrations compared to the MOPITT super-observations, the inversion applies negative increments to the prior emission estimates (Figure 2b). These negative increments mainly occur in fall and winter, even though there is a lower number of observations during these seasons compared to the spring and summer. The highest in-

crements are found over large cities and over industrial areas **(Figure 2b), where CO emissions are high (Figure 2a)**. This shows the potential of MOPITT data to provide some information over areas with strong anthropogenic CO emissions

The differences between the prior and posterior CO annual budgets for 30 European countries are shown in **Table 2** for the year 2015. Annual budgets of the national emissions are decreased by about 1-11% **(Table 2)**. Similarly, the national and annual increments from 2011 to 2021 range between -1%-11%. Overall, the posterior emission estimates are about 6.3% lower than the prior emissions for the European Union + United Kingdom (EU-27+UK) area in 2015. This indicates that the European CO emissions could be slightly overestimated in the TNO-GHGco-v3 inventory.

The 2011-2021 inversion makes it possible to evaluate the trends and compare them to the ones indicated by the inventories over the decade. As our prior estimates of the emissions for 2020 and 2021 are set at the values for 2019 (see Section 2), trends of CO emissions are only computed from 2011 to 2019. This restriction avoids including the COVID-19 pandemic years.

The TNO-GHGco-v3 CO emissions show a decreasing trend over EU-27+UK area from 2011 to 2019 (Figure 1), of about -2.5%/year ($p=9.5 \times 10^{-4}$). These decreasing trends are mainly driven by the transport sector (Zheng et al., 2019) with progressive pollution control on vehicles that has cut down CO European emissions (Crippa et al., 2016). Interestingly, the trends from 2011 to 2019 in the TNO inventory, based on the EMEP official reporting, exhibit some disparities depending on the countries with for example, a stronger decreasing trend over France than over Germany.

The posterior CO emissions display a very similar decreasing trend than the prior emissions over the EU-27+UK area (Figure 1) of about -2.2 %/year ($p=2.2 \times 10^{-3}$). The main differences between the prior and posterior trends are found for the autumn and winter months, with a posterior trend of about -1.9%/year compared to the prior trend of about -2.4%/year. Spatially, the differences are larger in Italy, in Czech Republic and in the Balkans than in the rest of Europe (Figure 6). While the TNO-GHGco-v3 inventory shows significant decreasing trends in these regions, the posterior emissions **appear to be stagnating, with even non significative increasing trend over parts of Italy**. These areas benefit from the best MOPITT coverage, with the highest number of MOPITT super-observations (Figure 5a). Consequently, the assimilation of MOPITT

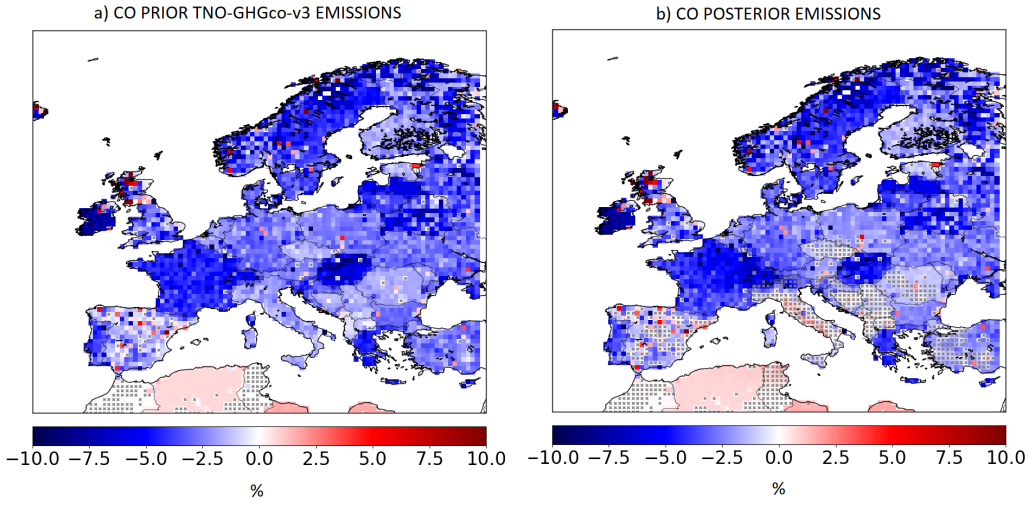

Figure 6. *Trends of CO emissions from 2011 to 2019 (a) in the TNO-GHGco-v3 inventory and b) in the posterior emissions, in %/yr. Crosses show pixels with insignificant trend (p-value higher than 0.05).*

observations in the inversions attenuates the strong decreasing trend of the CO emissions in the TNO-GHGco-v3 inventory, particularly during autumn and winter.

Finally, there is no significant inter-annual variability from 2011 to 2019, neither in the prior nor in the posterior CO emissions. A particular attention has consequently been put on the possible detection of an inter-annual anomaly linked to the policies implemented in response to the COVID-19 in 2020.

3.3 Impact of COVID-19

Following a usual diagnostic in the literature to assess the change in air pollutants concentrations due to the COVID-19 policies, we characterize the impact of the COVID-19 policies in terms of change of emissions budgets from April 2019 to April 2020. Most of the European countries implemented lock-down policies in April, after a progressive implementation of the national lock-downs from 9 March 2020 (Italy) to 23 March 2020 (United Kingdom, UK). The change from April 2019 to April 2020 potentially includes variations associated to drivers of the usual emission processes (e.g. changes of temperature from 2019 to 2020) but as indicated above, the typical inter-annual variations in both the prior and posterior estimates are relatively small. Since the

prior estimates for 2020 and 2019 are identical (see Section 2), we actually analyze the impact of the COVID-19 policies in terms of differences of increments provided by the inversions to these prior estimates between April 2019 and April 2020. Overall a much smaller lock-down-driven impact is expected for CO than for NO_2, particularly because of smaller contributions from lock-down-affected sources (Clark et al., 2021).

At the European scale, the CO posterior emission estimates derived from the MOPITT data decrease by about -1.3% in April 2020 compared to April 2019 (Table 3). This decrease is lower than the estimates of about -4.7%, -6.4%, -7.6% and -8.2% of, respectively, Guevara et al. (2023), Doumbia et al. (2021), Forster et al. (2021) and from the officially reported emissions from EMEP/CEIP (CEIP, 2022).

Nevertheless, as shown in Figure 7, the inversions lead to a higher decrease of CO emissions over the areas where the anthropogenic emissions are usually large, and particularly over industrial basins such as over the Benelux/Rhine-Rhur Valley where the decrease reaches -8% and over the Po Valley where it reaches -10% in April 2020 compared to April 2019 (Figure 7c).

4 Discussion and Conclusion

The CIF, coupled to the regional chemistry-transport model CHIMERE and its adjoint, and the satellite CO MOPITT data have been used to estimate 11 years from 2011 to 2021 of European CO emissions. The analysis of the inversion results reveal the challenges associated with the inversion of CO emissions at the regional scale over Europe. Annual budgets of the national emissions are decreased by about 1-11% over the decade and over Europe. These decreases are mainly due to negative corrections during autumn and winter.

The posterior CO emissions display a very similar decreasing trend than the prior emissions over the EU-27+UK area with a trend of about -2.2 %/year, showing a general consistency with reported anthropogenic emissions. This trend is slightly lower than in the prior emissions. The assimilation of the MOPITT observation in the inversions indeed attenuate the decreasing trend of the CO emissions in the TNO inventory over areas benefiting from the highest number of MOPITT super-observations (particularly over Italy and over the Balkans), and particularly in autumn and winter.

The posterior simulation still presents positive biases compared to the observations. **The minimization algorithm of the inversion appears to converge correctly with the constraints used**

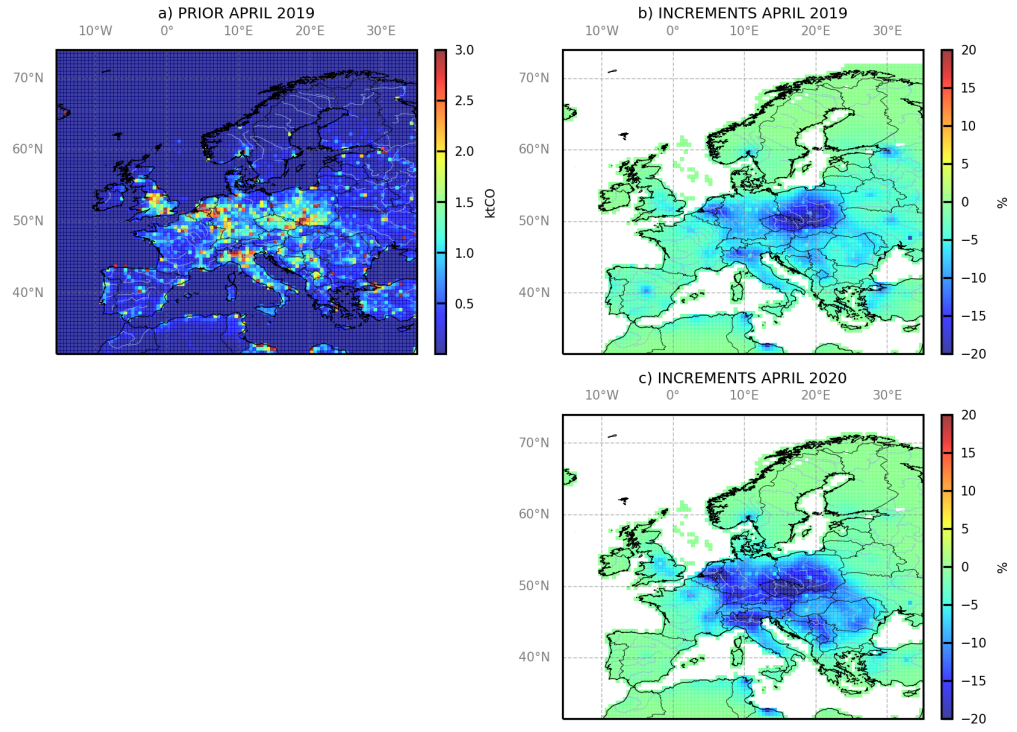

Figure 7. a) Emissions estimated by the TNO inventory in April 2019, in ktCO/month. Increment provided by the inversions in b) April 2019 and c) April 2020, in %.

in practice. Therefore, these residual positive biases can mainly be explained for a large part by the large errors associated to the observations in our inversion framework. As discussed in Section 2.2, our derivation of the error associated with each super-observation is conservative. Other indices support this assumption. In particular, the χ^2 diagnostic (Ménard and Chang, 2000) is significantly lower than 1. This indicates that the B and R matrices used here to characterize the prior and observation errors likely overestimate the amplitude of these errors (Ménard and Chang, 2000). However, even if assuming that the observation errors would only consist in random noise uncorrelated in space and setting the error on the super-observation as that of the average of the number of observations $nobs$ in the model grid cells, i.e. of the order of $\frac{1}{\sqrt{(nobs)}}$ times the observation error for individual observations, the impact would be moderate since $nobs$ is generally equal to 2 to 3. Actually, the

set-up of the B matrix is also rather conservative, and the balance between the two errors in the set-up of the B and R matrices may be relatively good. Therefore, the lack of fit to the observations in these inversions could be associated to the large retrieval error corresponding to the MOPITT product. The robustness of the inversions would still benefit from a refinement of our configuration of the R matrix which would lead to a better fit to the observations. First, we should probably investigate the components of the retrieval errors which are distributed along with the MOPITT product. Gaubert et al. (2023) indicate that when applying the averaging kernel, the smoothing error could be ignored and that the weight of this component is significant. The revision of our conservative assignment of the observation errors to the super-observation would be more challenging. It would require a good knowledge of the respective weight of the random noise (without spatial correlation) and of the systematic errors (with spatial correlations) in the total retrieval errors, as well as a good knowledge of the typical correlation length scales of the systematic errors, while we lack of insights regarding this. The use of notional assumptions (as for the characterization of the model error) may still represent a sensible trade-off and allow for an improved assimilation of the observations. Finally, a refinement of the inversion strategy may **also** support a better fit to the observations. In particular, under the assumptions that uncertainties in the control variables have a Gaussian distribution, the control of the logarithm of the emissions rather than of scaling factor for these emissions may better correspond to our CO inversion problem, in which CO emissions are necessarily positive, but in which these emissions could have to be strongly decreased. Opposed to the Gaussian characterization and to the spatial correlation of the uncertainties in the emissions, the Gaussian characterization and the spatial correlation of the uncertainties in logarithm of the emissions could increase the flexibility for large local corrections of the emissions. The current characterization of the uncertainties in the CO emissions using a Gaussian distribution may actually contribute to the limitation of the fit to the observations.

The small corrections of the CO emissions at national scales by the inversion can be attributed, first, to the general consistency between the TNO-GHGco-v3 inventory and the satellite data. However, analysis of specific patterns such as the impact of the covid-19 crisis reveal that it can also be seen as a lack of observation constraint to adjust the prior estimate of the emissions. The large errors **associated to the observations in our inversion framework**, and the lack of data over large parts of Europe are definitely some sources of limitation on the observational constraint.

However, in a more general way, this questions the ability to exploit large scale variations in the CO satellite data to constrain regional and national to continental scale budgets of the emissions. Emission hot spots generate a relatively strong local signal, which is much better caught and exploited by the inversions than the larger scale signals, despite the moderate spatial resolution of the MOPITT data. This is why the corrections of these hot spot emissions are stronger and more convincing than the corrections of the national and continental scale emissions, as shown by the analysis of the impact of covid-19 policies. Accurate monitoring of the national anthropogenic CO emissions will likely rely more on the aggregation of local emission monitoring data rather than on the processing of large scale variations in the CO fields. The former requires modeling and inversion systems at spatial resolution finer than those used here, as well satellite images at high spatial resolution. The CO images of the TROPOMI instrument onboard the Sentinel-5P mission with a 5.5km x7 km resolution since August 2019 should be well suited for such a perspective. The large increase in the number of observations with this mission is expected to increase the capabilities to monitor CO emissions and to address air-quality-related emissions at the national to subnational scales.

5 Open Research

MOPITT version 8 products are freely available through NASA's EarthData portal at https://earthdata.nasa.gov/, (Deeter et al., 2019). The TNO-GHGco-v3 inventory (Super et al., 2020) is available upon request from TNO (contact: Hugo Denier van der Gon, hugo.deniervandergon@tno.nl).The CHIMERE code is available here: www.lmd.polytechnique.fr/chimere/, (Menut et al., 2013; Mailler et al., 2017). The CIF inversion system (Berchet et al., 2021) is available at : http://community-inversion.eu/

Acknowledgements. We acknowledge the NCAR MOPITT group for the production of the CO retrievals. **A large part of the development and analysis were conducted in the frame of the H2020 VERIFY and COCO2 projects, funded by the European Commission Horizon 2020 research and innovation programme, respectively under agreement number 776810 and 958927**. We wish to thank all the persons involved in the preparation, coordination and management of these projects. This study has also received funding from the French ANR project ARGONAUT under grant agreement No ANR-19-CE01-0007 and from the French PRIMEQUAL project LOCKAIR under grant agreement No 2162D0010. This work was

supported by the CNES (Centre National d'Etudes Spatiales), in the frame of the TOSCA ARGOS project. This work was granted access to the HPC resources of TGCC under the allocations A0100102201 and A0110102201 made by GENCI. Finally, we wish to thank J. Bruna (LSCE) and his team for computer support.

The authors declare that they have no conflict of interest.

Country Code	Difference between CO anthropogenic emissions estimates from the inversions and TNO-GHGco-v3 in %
ALB	-5.9
AUT	-8.0
BEL	-6.2
BLR	-0.6
CHE	-8.4
DEU	-7.6
DNK	-1.2
ESP	-4.1
FIN	-0.5
FRA	-5.3
GBR	-3.3
IRL	-0.8
ITA	-11.4
LUX	-6.3
NLD	-6.8
NOR	-1.0
PRT	-3.0
SWE	-0.4
BGR	-4.0
CZE	-10.6
EST	-0.3
HRV	8.94
HUN	-7.1
LTU	-0.7
LVA	-0.4
POL	-6.7
ROU	-5.6
SVN	-9.1
SVK	-7.8
UKR	-3.4
EU-27+UK	-6.3

Table 2. Difference between the CO annual emissions from the TNO-GHGco-v3 inventory used as prior in this study and from the inversions, by country, in %, in 2015.

Country Code	Difference between CO posterior emissions estimates in April 2020 and in April 2019 in %
BEL	-5.6
CHE	-3.5
DEU	-7.3
FRA	-1.2
GBR	-0.4
ITA	-3.5
LUX	-5.4
NLD	-7.7
EU-27+UK	-1.3

Table 3. Difference between the CO posterior emissions in April 2020 and in April 2019, by country, in %.

References

Arellano, J., F., A., Kasibhatla, P. S., Giglio, L., van der Werf, G. R., Randerson, J. T., and Collatz, G. J.: Time-dependent inversion estimates of global biomass-burning CO emissions using Measurement of Pollution in the Troposphere (MOPITT) measurements, Journal of Geophysical Research: Atmospheres, 111, https://doi.org/https://doi.org/10.1029/2005JD006613, 2006.

Aumann, H., Chahine, M., Gautier, C., Goldberg, M., Kalnay, E., McMillin, L., Revercomb, H., Rosenkranz, P., Smith, W., Staelin, D., Strow, L., and Susskind, J.: AIRS/AMSU/HSB on the Aqua mission: design, science objectives, data products, and processing systems, IEEE Transactions on Geoscience and Remote Sensing, 41, 253–264, https://doi.org/10.1109/TGRS.2002.808356, 2003.

Beer, R.: TES on the aura mission: scientific objectives, measurements, and analysis overview, IEEE Transactions on Geoscience and Remote Sensing, 44, 1102–1105, https://doi.org/10.1109/TGRS.2005.863716, 2006.

Berchet, A., Sollum, E., Thompson, R. L., Pison, I., Thanwerdas, J., Broquet, G., Chevallier, F., Aalto, T., Berchet, A., Bergamaschi, P., Brunner, D., Engelen, R., Fortems-Cheiney, A., Gerbig, C., Groot Zwaaftink, C. D., Haussaire, J.-M., Henne, S., Houweling, S., Karstens, U., Kutsch, W. L., Luijkx, I. T., Monteil, G., Palmer, P. I., van Peet, J. C. A., Peters, W., Peylin, P., Potier, E., Rödenbeck, C., Saunois, M., Scholze, M., Tsuruta, A., and Zhao, Y.: The Community Inversion Framework v1.0: a unified system for atmospheric inversion studies, Geoscientific Model Development, 14, 5331–5354, https://doi.org/10.5194/gmd-14-5331-2021, 2021.

Bieser, J., Aulinger, A., Matthias, V., Quante, M., and Denier van der Gon, H.: Vertical emission profiles for Europe based on plume rise calculations, Environmental Pollution, 159, 2935–2946, https://doi.org/https://doi.org/10.1016/j.envpol.2011.04.030, nitrogen Deposition, Critical Loads and Biodiversity, 2011.

Buchholz, R. R., Deeter, M. N., Worden, H. M., Gille, J., Edwards, D. P., Hannigan, J. W., Jones, N. B., Paton-Walsh, C., Griffith, D. W. T., Smale, D., Robinson, J., Strong, K., Conway, S., Sussmann, R., Hase, F., Blumenstock, T., Mahieu, E., and Langerock, B.: Validation of MOPITT carbon monoxide using ground-based Fourier transform infrared spectrometer data from NDACC, Atmospheric Measurement Techniques, 10, 1927–1956, https://doi.org/10.5194/amt-10-1927-2017, 2017.

Buchholz, R. R., Worden, H. M., Park, M., Francis, G., Deeter, M. N., Edwards, D. P., Emmons, L. K., Gaubert, B., Gille, J., Martínez-Alonso, S., Tang, W., Kumar, R., Drummond, J. R., Clerbaux, C., George, M., Coheur, P.-F., Hurtmans, D., Bowman, K. W., Luo, M., Payne, V. H., Worden, J. R., Chin, M., Levy, R. C., Warner, J., Wei, Z., and Kulawik, S. S.: Air pollution trends measured from Terra: CO and AOD over industrial, fire-prone, and background regions, Remote Sensing of Environment, 256, 112 275, https://doi.org/https://doi.org/10.1016/j.rse.2020.112275, 2021.

CEIP: EMEP Centre on Emissions Inventories and Projections, Officially reported emission data, Tech. rep., https://www.ceip.at/webdab-emission-database/reported-emissiondata, 2022.

Chevallier, F., Fortems, A., Bousquet, P., Pison, I., Szopa, S., Devaux, M., and Hauglustaine, D. A.: African CO emissions between years 2000 and 2006 as estimated from MOPITT observations, Biogeosciences, 6, 103–111, https://doi.org/10.5194/bg-6-103-2009, 2009.

CHIMERE: Documentation of the chemistry-transport model CHIMERE, Tech. rep., https://www.lmd.polytechnique.fr/chimere/docs/CHIMEREdoc2017.pdf, 2017.

Clark, H., Bennouna, Y., Tsivlidou, M., Wolff, P., Sauvage, B., Barret, B., Le Flochmoën, E., Blot, R., Boulanger, D., Cousin, J.-M., Nédélec, P., Petzold, A., and Thouret, V.: The effects of the COVID-19 lockdowns on the composition of the troposphere as seen by In-service Aircraft for a Global Observing System (IAGOS) at Frankfurt, Atmospheric Chemistry and Physics, 21, 16 237–16 256, https://doi.org/10.5194/acp-21-16237-2021, 2021.

Clerbaux, C., Boynard, A., Clarisse, L., George, M., Hadji-Lazaro, J., Herbin, H., Hurtmans, D., Pommier, M., Razavi, A., Turquety, S., Wespes, C., and Coheur, P.-F.: Monitoring of atmospheric composition using the thermal infrared IASI/MetOp sounder, Atmospheric Chemistry and Physics, 9, 6041–6054, https://doi.org/10.5194/acp-9-6041-2009, 2009.

Crippa, M., Janssens-Maenhout, G., Dentener, F., Guizzardi, D., Sindelarova, K., Muntean, M., Van Dingenen, R., and Granier, C.: Forty years of improvements in European air quality: regional policy-industry interactions with global impacts, Atmospheric Chemistry and Physics, 16, 3825–3841, https://doi.org/10.5194/acp-16-3825-2016, 2016.

Deeter, M.: MOPITT Version 8 Product User's Guide, Tech. rep., https://www2.acom.ucar.edu/sites/default/files/documents/v8_users_guide_201812.pdf, 2018.

Deeter, M. N., Emmons, L. K., Francis, G. L., Edwards, D. P., Gille, J. C., Warner, J. X., Khattatov, B., Ziskin, D., Lamarque, J.-F., Ho, S.-P., Yudin, V., Attié, J.-L., Packman, D., Chen, J., Mao, D., and Drummond, J. R.: Operational carbon monoxide retrieval algorithm and selected results for the MOPITT instrument, Journal of Geophysical Research: Atmospheres, 108, https://doi.org/https://doi.org/10.1029/2002JD003186, 2003.

Deeter, M. N., Martínez-Alonso, S., Edwards, D. P., Emmons, L. K., Gille, J. C., Worden, H. M., Pittman, J. V., Daube, B. C., and Wofsy, S. C.: Validation of MOPITT Version 5 thermal-infrared, near-infrared, and multispectral carbon monoxide profile retrievals for 2000–2011, Journal of Geophysical Research: Atmospheres, 118, 6710–6725, https://doi.org/https://doi.org/10.1002/jgrd.50272, 2013.

Deeter, M. N., Edwards, D. P., Francis, G. L., Gille, J. C., Mao, D., Martínez-Alonso, S., Worden, H. M., Ziskin, D., and Andreae, M. O.: Radiance-based retrieval bias mitigation for the MOPITT instrument: the

version 8 product, Atmospheric Measurement Techniques, 12, 4561–4580, https://doi.org/10.5194/amt-12-4561-2019, 2019.

Denier van der Gon, H., Dellaert, S., I. Super, J. K., and Visschedijk, A.: Final High Resolution emission data 2005-2018, Tech. rep., https://verify.lsce.ipsl.fr/images/PublicDeliverables/VERIFY_D2_3_TNO_v1.pdf, 2021.

Doumbia, T., Granier, C., Elguindi, N., Bouarar, I., Darras, S., Brasseur, G., Gaubert, B., Liu, Y., Shi, X., Stavrakou, T., Tilmes, S., Lacey, F., Deroubaix, A., and Wang, T.: Changes in global air pollutant emissions during the COVID-19 pandemic: a dataset for atmospheric modeling, Earth System Science Data, 13, 4191–4206, https://doi.org/10.5194/essd-13-4191-2021, 2021.

Drummond, J. R., Mand, G., and Bailak, G. V.: Calibration of the MOPITT instrument for EOS, in: Optics + Photonics, 1996.

Forster, P., Forster, H., and Evans, M. e. a.: Current and future global climate impacts resulting from COVID-19, Nat. Clim. Chang., 10, 913–919, https://doi.org/10.1038/s41558-020-0883-0, 2021.

Fortems-Cheiney, A., Chevallier, F., Pison, I., Bousquet, P., Szopa, S., Deeter, M. N., and Clerbaux, C.: Ten years of CO emissions as seen from Measurements of Pollution in the Troposphere (MOPITT), Journal of Geophysical Research: Atmospheres, 116, https://doi.org/https://doi.org/10.1029/2010JD014416, 2011a.

Fortems-Cheiney, A., Chevallier, F., Pison, I., Bousquet, P., Szopa, S., Deeter, M. N., and Clerbaux, C.: Ten years of CO emissions as seen from Measurements of Pollution in the Troposphere (MOPITT), Journal of Geophysical Research: Atmospheres, 116, https://doi.org/https://doi.org/10.1029/2010JD014416, 2011b.

Fortems-Cheiney, A., Chevallier, F., Pison, I., Bousquet, P., Saunois, M., Szopa, S., Cressot, C., Kurosu, T. P., Chance, K., and Fried, A.: The formaldehyde budget as seen by a global-scale multi-constraint and multi-species inversion system, Atmospheric Chemistry and Physics, 12, 6699–6721, https://doi.org/10.5194/acp-12-6699-2012, 2012.

Fortems-Cheiney, A., Pison, I., Broquet, G., Dufour, G., Berchet, A., Potier, E., Coman, A., Siour, G., and Costantino, L.: Variational regional inverse modeling of reactive species emissions with PYVAR-CHIMERE-v2019, Geoscientific Model Development, 14, 2939–2957, https://doi.org/10.5194/gmd-14-2939-2021, 2021.

Gaubert, B., Emmons, L. K., Raeder, K., Tilmes, S., Miyazaki, K., Arellano Jr., A. F., Elguindi, N., Granier, C., Tang, W., Barré, J., Worden, H. M., Buchholz, R. R., Edwards, D. P., Franke, P., Anderson, J. L., Saunois, M., Schroeder, J., Woo, J.-H., Simpson, I. J., Blake, D. R., Meinardi, S., Wennberg, P. O., Crounse, J., Teng, A., Kim, M., Dickerson, R. R., He, H., Ren, X., Pusede, S. E., and Diskin, G. S.: Correcting model biases of CO in East Asia: impact on oxidant distributions during KORUS-AQ, Atmospheric Chemistry and Physics, 20, 14 617–14 647, https://doi.org/10.5194/acp-20-14617-2020, 2020.

Gaubert, B., Edwards, D. P., Anderson, J. L., Arellano, A. F., Barré, J., Buchholz, R. R., Darras, S., Emmons, L. K., Fillmore, D., Granier, C., Hannigan, J. W., Ortega, I., Raeder, K., Soulié, A., Tang, W., Worden, H. M., and Ziskin, D.: Global Scale Inversions from MOPITT CO and MODIS AOD, Remote Sensing, 15, https://doi.org/10.3390/rs15194813, 2023.

George, M., Clerbaux, C., Bouarar, I., Coheur, P.-F., Deeter, M. N., Edwards, D. P., Francis, G., Gille, J. C., Hadji-Lazaro, J., Hurtmans, D., Inness, A., Mao, D., and Worden, H. M.: An examination of the long-term CO records from MOPITT and IASI: comparison of retrieval methodology, Atmospheric Measurement Techniques, 8, 4313–4328, https://doi.org/10.5194/amt-8-4313-2015, 2015.

Gilbert, J. and Lemaréchal, C.: Some numerical experiments with variable storage quasi Newton algorithms, Math. Program., 45, 407–435, https://doi.org/10.1007/BF01589113, 1989.

Guenther, A., Karl, T., Harley, P., Wiedinmyer, C., Palmer, P. I., and Geron, C.: Estimates of global terrestrial isoprene emissions using MEGAN (Model of Emissions of Gases and Aerosols from Nature), Atmospheric Chemistry and Physics, 6, 3181–3210, https://doi.org/10.5194/acp-6-3181-2006, 2006.

Guevara, M., Petetin, H., Jorba, O., Denier van der Gon, H., Kuenen, J., Super, I., Granier, C., Doumbia, T., Ciais, P., Liu, Z., Lamboll, R. D., Schindlbacher, S., Matthews, B., and Pérez García-Pando, C.: Towards near-real time air pollutant and greenhouse gas emissions: lessons learned from multiple estimates during the COVID-19 Pandemic, EGUsphere, 2023, 1–36, https://doi.org/10.5194/egusphere-2023-186, 2023.

Hooghiemstra, P. B., Krol, M. C., van Leeuwen, T. T., van der Werf, G. R., Novelli, P. C., Deeter, M. N., Aben, I., and Röckmann, T.: Interannual variability of carbon monoxide emission estimates over South America from 2006 to 2010, Journal of Geophysical Research: Atmospheres, 117, https://doi.org/https://doi.org/10.1029/2012JD017758, 2012.

Jiang, Z., Jones, D. B. A., Kopacz, M., Liu, J., Henze, D. K., and Heald, C.: Quantifying the impact of model errors on top-down estimates of carbon monoxide emissions using satellite observations, Journal of Geophysical Research: Atmospheres, 116, https://doi.org/https://doi.org/10.1029/2010JD015282, 2011.

Jiang, Z., Jones, D. B. A., Worden, J., Worden, H. M., Henze, D. K., and Wang, Y. X.: Regional data assimilation of multi-spectral MOPITT observations of CO over North America, Atmospheric Chemistry and Physics, 15, 6801–6814, https://doi.org/10.5194/acp-15-6801-2015, 2015.

Jiang, Z., Worden, J. R., Worden, H., Deeter, M., Jones, D. B. A., Arellano, A. F., and Henze, D. K.: A 15-year record of CO emissions constrained by MOPITT CO observations, Atmospheric Chemistry and Physics, 17, 4565–4583, https://doi.org/10.5194/acp-17-4565-2017, 2017.

Jones, D. B. A., Bowman, K. W., Logan, J. A., Heald, C. L., Liu, J., Luo, M., Worden, J., and Drummond, J.: The zonal structure of tropical O_3 and CO as observed by the Tropospheric Emission Spectrometer in November 2004 – Part 1: Inverse modeling of CO emissions, Atmospheric Chemistry and Physics, 9, 3547–3562, https://doi.org/10.5194/acp-9-3547-2009, 2009.

Konovalov, I. B., Berezin, E. V., Ciais, P., Broquet, G., Zhuravlev, R. V., and Janssens-Maenhout, G.: Estimation of fossil-fuel CO_2 emissions using satellite measurements of "proxy" species, Atmospheric Chemistry and Physics, 16, 13 509–13 540, https://doi.org/10.5194/acp-16-13509-2016, 2016.

Kopacz, M., Jacob, D. J., Fisher, J. A., Logan, J. A., Zhang, L., Megretskaia, I. A., Yantosca, R. M., Singh, K., Henze, D. K., Burrows, J. P., Buchwitz, M., Khlystova, I., McMillan, W. W., Gille, J. C., Edwards, D. P., Eldering, A., Thouret, V., and Nedelec, P.: Global estimates of CO sources with high resolution by adjoint inversion of multiple satellite datasets (MOPITT, AIRS, SCIAMACHY, TES), Atmospheric Chemistry and Physics, 10, 855–876, https://doi.org/10.5194/acp-10-855-2010, 2010.

Kuenen, J. and Dore, C.: EMEP/EEA air pollutant emission inventory guidebook 2019: Uncertainties, Tech. rep., https://www.eea.europa.eu/publications/emep-eea-guidebook-2019/part-a-general-guidance-chapters/5-uncertainties, 2019.

Kuenen, J., Dellaert, S., Visschedijk, A., Jalkanen, J.-P., Super, I., and Denier van der Gon, H.: CAMS-REG-v4: a state-of-the-art high-resolution European emission inventory for air quality modelling, Earth System Science Data, 14, 491–515, https://doi.org/10.5194/essd-14-491-2022, 2022.

Lelieveld, J., Gromov, S., Pozzer, A., and Taraborrelli, D.: Global tropospheric hydroxyl distribution, budget and reactivity, Atmospheric Chemistry and Physics, 16, 12 477–12 493, https://doi.org/10.5194/acp-16-12477-2016, 2016.

Mailler, S., Menut, L., Khvorostyanov, D., Valari, M., Couvidat, F., Siour, G., Turquety, S., Briant, R., Tuccella, P., Bessagnet, B., Colette, A., Létinois, L., Markakis, K., and Meleux, F.: CHIMERE-2017: from urban to hemispheric chemistry-transport modeling, Geoscientific Model Development, 10, 2397–2423, https://doi.org/10.5194/gmd-10-2397-2017, 2017.

McMillan, W. W., Barnet, C., Strow, L., Chahine, M. T., McCourt, M. L., Warner, J. X., Novelli, P. C., Korontzi, S., Maddy, E. S., and Datta, S.: Daily global maps of carbon monoxide from NASA's Atmospheric Infrared Sounder, Geophysical Research Letters, 32, https://doi.org/https://doi.org/10.1029/2004GL021821, 2005.

Menut, L., Bessagnet, B., Khvorostyanov, D., Beekmann, M., Blond, N., Colette, A., Coll, I., Curci, G., Foret, G., Hodzic, A., Mailler, S., Meleux, F., Monge, J.-L., Pison, I., Siour, G., Turquety, S., Valari, M., Vautard, R., and Vivanco, M. G.: CHIMERE 2013: a model for regional atmospheric composition modelling, Geoscientific Model Development, 6, 981–1028, https://doi.org/10.5194/gmd-6-981-2013, 2013.

Miyazaki, K., Eskes, H. J., and Sudo, K.: A tropospheric chemistry reanalysis for the years 2005–2012 based on an assimilation of OMI, MLS, TES, and MOPITT satellite data, Atmospheric Chemistry and Physics, 15, 8315–8348, https://doi.org/10.5194/acp-15-8315-2015, 2015.

Ménard, R. and Chang, L.-P.: Assimilation of Stratospheric Chemical Tracer Observations Using a Kalman Filter. Part II: χ2-Validated Results and Analysis of Variance and Correlation Dynamics, Monthly Weather Review, 128, 2672 – 2686, https://doi.org/https://doi.org/10.1175/1520-0493(2000)128<2672:AOSCTO>2.0.CO;2, 2000.

Owens, R. G. and Hewson, T.: ECMWF Forecast User Guide, Tech. rep., https://doi.org/https://doi.org/10.21957/m1cs7h, 2018.

Prather, M. J.: Time scales in atmospheric chemistry: Theory, GWPs for CH4 and CO, and runaway growth, Geophysical Research Letters, 23, 2597–2600, https://doi.org/https://doi.org/10.1029/96GL02371, 1996.

Pétron, G., Granier, C., Khattatov, B., Lamarque, J.-F., Yudin, V., Müller, J.-F., and Gille, J.: Inverse modeling of carbon monoxide surface emissions using Climate Monitoring and Diagnostics Laboratory network observations, Journal of Geophysical Research: Atmospheres, 107, ACH 10–1–ACH 10–23, https://doi.org/https://doi.org/10.1029/2001JD001305, 2002.

Qu, Z., Henze, D. K., Worden, H. M., Jiang, Z., Gaubert, B., Theys, N., and Wang, W.: Sector-Based Top-Down Estimates of NOx, SO2, and CO Emissions in East Asia, Geophysical Research Letters, 49, e2021GL096 009, https://doi.org/https://doi.org/10.1029/2021GL096009, e2021GL096009 2021GL096009, 2022.

Rayner, P. J., Michalak, A. M., and Chevallier, F.: Fundamentals of data assimilation applied to biogeochemistry, Atmospheric Chemistry and Physics, 19, 13 911–13 932, https://doi.org/10.5194/acp-19-13911-2019, 2019.

San-Miguel-Ayanz, J. and Steinbrecher, R.: EMEP/EEA air pollutant emission inventory guidebook 2019: Forest and other vegetation fires, Tech. rep., https://www.eea.europa.eu/publications/emep-eea-guidebook-2019/part-b-sectoral-guidance-chapters/11-natural-sources/11-b-forest-fires/view, 2019.

Stein, O., Schultz, M. G., Bouarar, I., Clark, H., Huijnen, V., Gaudel, A., George, M., and Clerbaux, C.: On the wintertime low bias of Northern Hemisphere carbon monoxide found in global model simulations, Atmospheric Chemistry and Physics, 14, 9295–9316, https://doi.org/10.5194/acp-14-9295-2014, 2014.

Strode, S. A., Duncan, B. N., Yegorova, E. A., Kouatchou, J., Ziemke, J. R., and Douglass, A. R.: Implications of carbon monoxide bias for methane lifetime and atmospheric composition in chemistry climate models, Atmospheric Chemistry and Physics, 15, 11 789–11 805, https://doi.org/10.5194/acp-15-11789-2015, 2015.

Super, I., Dellaert, S. N. C., Visschedijk, A. J. H., and Denier van der Gon, H. A. C.: Uncertainty analysis of a European high-resolution emission inventory of CO_2 and CO to support inverse modelling and network design, Atmospheric Chemistry and Physics, 20, 1795–1816, https://doi.org/10.5194/acp-20-1795-2020, 2020.

Szopa, S.and Foret, G. M. L. C. A.: Impact of large scale circulation on European summer surface ozone: consequences for modeling, Atmospheric Environment, 43, https://doi.org/doi:10.1016/j.atmosenv.2008.10.0390, 2008.

Valin, L. C., Russell, A. R., Hudman, R. C., and Cohen, R. C.: Effects of model resolution on the interpretation of satellite NO_2 observations, Atmospheric Chemistry and Physics, 11, 11 647–11 655, https://doi.org/10.5194/acp-11-11647-2011, 2011.

Vestreng, V., Breivik, K.and Adams, M., Wagner, A., Goodwin, J., Rozovskaya, O., and Oacyna, J.: Inventory Review 2005 - Emission Data reported to CLRTAP and under the NEC Direc-tive - Initial review for HMs and POPs, Tech. rep., 2005.

Worden, H. M., Deeter, M. N., Edwards, D. P., Gille, J. C., Drummond, J. R., and Nédélec, P.: Observations of near-surface carbon monoxide from space using MOPITT multispectral retrievals, Journal of Geophysical Research: Atmospheres, 115, https://doi.org/https://doi.org/10.1029/2010JD014242, 2010.

Yin, Y., Chevallier, F., Ciais, P., Broquet, G., Fortems-Cheiney, A., Pison, I., and Saunois, M.: Decadal trends in global CO emissions as seen by MOPITT, Atmospheric Chemistry and Physics, 15, 13 433–13 451, https://doi.org/10.5194/acp-15-13433-2015, 2015.

Yumimoto, K. and Uno, I.: Adjoint inverse modeling of CO emissions over Eastern Asia using four-dimensional variational data assimilation, Atmospheric Environment, 40, 6836–6845, https://doi.org/https://doi.org/10.1016/j.atmosenv.2006.05.042, 2006.

Zheng, B., Chevallier, F., Ciais, P., Yin, Y., Deeter, M. N., Worden, H. M., Wang, Y., Zhang, Q., and He, K.: Rapid decline in carbon monoxide emissions and export from East Asia between years 2005 and 2016, Environmental Research Letters, 13, 044 007, https://doi.org/10.1088/1748-9326/aab2b3, 2018.

Zheng, B., Chevallier, F., Yin, Y., Ciais, P., Fortems-Cheiney, A., Deeter, M. N., Parker, R. J., Wang, Y., Worden, H. M., and Zhao, Y.: Global atmospheric carbon monoxide budget 2000–2017 inferred from multi-species atmospheric inversions, Earth System Science Data, 11, 1411–1436, https://doi.org/10.5194/essd-11-1411-2019, 2019.